



Flexible FTIR Spectral Imaging Enhancement for Industrial Robot Infrared Vision Sensing

Tingting Liu, *Student Member, IEEE*, Hai Liu , *Member, IEEE*, You-Fu Li , *Senior Member, IEEE*, Zengzhao Chen, Zhaoli Zhang, *Member, IEEE*, and Sannyuya Liu

Abstract—Infrared (IR) spectral imaging sensing is a powerful visual technique for industrial material recognition in robot vision systems. However, the imaging sensing data have issues of random noise and band overlap. Resolution enhancement is usually the first step in the preprocessing procedure of industrial robot vision sensing. In this article, we develop a resolution-enhancement algorithm with total variation (TV) constraints for the degraded Fourier transform IR (FTIR) spectrum due to overlap and noise degradation in the robot vision sensing. The kernel function is calculated using the spectrometer imaging systems and Fourier optical theory. The proposed model not only can remove noises effectively but also can estimate the kernel function because of the adaptive TV as constraint regularization. This model is examined by a set of simulated FTIR spectra with the Poisson noises and a series of real FTIR spectra. The proposed model is compared with the other state-of-the-art methods in terms of performance. Experimental results demonstrate that the proposed approach can split the overlap band effectively while the spectral structure details are retained satisfactorily. The enhanced high-resolution imaging spectrum data can raise the robot vision sensing accuracy in industrial intelligent systems.

Index Terms—Infrared imaging spectrum, intelligent vision system, robot infrared vision sensing, visual tracking.

Manuscript received March 28, 2019; revised July 1, 2019; accepted July 10, 2019. Date of publication August 12, 2019; date of current version January 4, 2020. This work was supported in part by the National Key Research and Development Program of China under Grant 2017YFB1401300 and Grant 2017YFB1401303, in part by the National Natural Science Foundation of China under Grant 61875068, Grant 61873220, Grant 61673329, and Grant 61505064, in part by the Research Grants Council of Hong Kong under Project CityU 11205015 and Project CityU 11255716, and in part by the Fundamental Research Funds for the Central Universities under Grant CCNU18ZDPY10 and Grant 2017YBZZ009. Paper no. TII-19-1099. (Tingting Liu and Hai Liu contributed equally to this article.) (Corresponding author: Hai Liu.)

T. Liu is with the National Engineering Research Center for E-Learning, Central China Normal University, Wuhan 430079, China, and also with the School of Computer Science, Carnegie Mellon University, Pittsburgh, PA 15213 USA (e-mail: tingting3@andrew.cmu.edu).

H. Liu is with the National Engineering Research Center for E-Learning, Central China Normal University, Wuhan 430079, China, and also with the Department of Mechanical Engineering, City University of Hong Kong, Kowloon, Hong Kong (e-mail: hailiu0204@mail.ccnu.edu.cn).

Y.-Fu Li is with the Department of Mechanical Engineering, City University of Hong Kong, Kowloon, Hong Kong, and also with the City University of Hong Kong Shenzhen Research Institute, Shenzhen 518057, China.

Z. Chen, Z. Zhang, and S. Liu are with the National Engineering Research Center for E-Learning, Central China Normal University, Wuhan 430079, China.

Color versions of one or more of the figures in this article are available online at <http://ieeexplore.ieee.org>.

Digital Object Identifier 10.1109/TII.2019.2934728

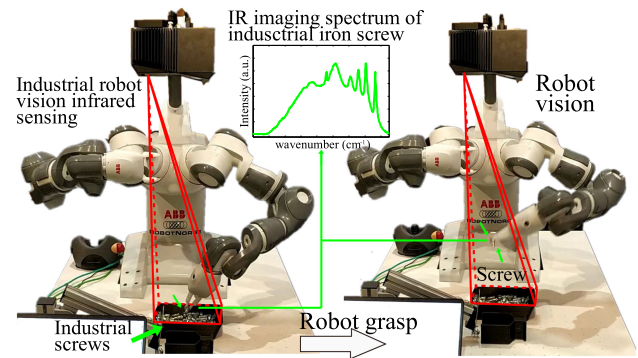


Fig. 1. Robotic limbs can finish the grasping task with the help of the FTIR spectrometer imaging sensing. The material component information of industrial iron screw can be captured by the robot vision IR spectrometer sensing instrument.

I. INTRODUCTION

INDUSTRIAL Fourier transform infrared (FTIR) imaging sensing is commonly applied in industrial material recognition [1]–[5], robot vision system [6]–[11], and remote sensing detection [12]–[15]. The FTIR spectrum can reveal the component on a molecular level and offers “fingerprint” spectral information to the component [16]–[18] in the robot vision sensing. Unfortunately, the FTIR spectrometers are often limited by band overlap, resolution degradation, and random noise; this condition influences the robot vision imaging quality of the infrared (IR) spectra [19], [20]. The spectral quality is also affected by the pressure and temperature of the robot vision sensing in the factory. The observed FTIR spectrum lines are easily misinterpreted under the above-mentioned factors, thereby influencing the recognition accuracy of the robot vision sensing. Therefore, the random noises in the FTIR imaging spectrum should be removed before the succeeding robot grasping processing. The traditional RGB-D camera [21], [22] in robot vision can only capture the shape and color information of screws for grasping task (see Fig. 1) [23]. However, the FTIR spectrometer sensing can capture the material component information, which can be used for assisting the setting of grasping control parameters. The spectral resolution-enhancement approach aims to explore the outstanding estimation of the high-resolution FTIR spectrum and its kernel function from the observed FTIR spectral lines.

To this end, various resolution-enhancement approaches are proposed to handle the problem of the Poissonian FTIR spectral imaging degradation in the robot vision sensing [24]–[31]. The

existing resolution-enhancement approaches can be categorized into the analysis prior-based approach (ANAP) and synthesis prior-based approach (SYNP). Wiener filtering [32] is a classic resolution-enhancement algorithm for the ANAP. Slima *et al.* [33], [34] developed the Kalman filter to improve the FTIR spectral resolution. This method has been used worldwide for industrial applications [35] to date. In [36], a homomorphic filter-based algorithm was proposed to raise the spectral resolution of the IR spectrum effectively. Then, the famous Fourier self-deconvolution (FSD) approach is developed and is an outstanding method in the robot IR vision sensing. The FSD approach requires the kernel function for all the resolution-enhancement tasks; thus, it is unsuitable for real circumstances. Lorentz-Fonfria and Padrós [37] sufficiently examined the several kernel functions that are commonly used in the FSD approach to select the accurate ones. Bessel- and Gaussian-like functions were suggested due to their good performance in the FSD approach. Jansson and Crilly [38], [39] developed a relaxation weighted function to reconstruct the degraded IR spectrum and achieve impressive high-resolution results. Sarker *et al.* [40] proposed a resolution-enhancement algorithm for the robot vision sensing. In this approach, a low-pass filter is developed and used to remove the high-frequency random noises. However, this method can only suppress some specific spectral noises in the practical application. KutraSnik *et al.* [41] constructed an adjustable acousto-optical filter, which can suppress the mixture noises in the IR spectrum data, to increase the IR spectrum quality for achieving universal performance. However, this filter fails to process the IR spectrum with strong noises. Wiener estimation [42] approach, which can recover the missed structure as many as possible, is recently developed for spectra line with heavy noises.

Richardson–Lucy is a popular approach for the SYNP. However, this method often amplifies the FTIR spectral noises with the increase in the number of iterations [43], [44]. Deng *et al.* [45] elevated the FTIR resolution with a prior knowledge on the basis of total variation (TV) regularization to address the aforementioned problem. This approach preserves the terahertz imaging spectrum structure details effectively. The TV regularization has received increasing popularity due to its edge-preserving property by not over-penalizing discontinuities while smoothness is controlled [46]. Zhu *et al.* proposed a convex regularization [29], [47] with a spatially dependent regularization parameter to refine the FTIR spectrum. Liu *et al.* [48], [49] proposed to boost the spectral resolution by introducing adaptive Tikhonov regularization based on the spectral line structures to reduce the noises in plain areas and conserve the spectral band structure information. Several algorithms based on Ridgelet transform regularization have also been proposed to improve the spectral resolution [50], [51]. However, these methods cannot process the FTIR spectrum with the Poisson noises. Evidently, the FTIR spectral resolution still needs to be improved.

In this article, we develop a fast resolution-enhancement approach for the Poisson noise suppression and overlap the peak separation in the robot vision system. This approach requires nonprior knowledge about the background information

of the grasped object. The main contributions of this article are threefold.

- 1) Flexible TV-norm is used for the FTIR spectral resolution enhancement in the robot IR vision system for the first time. The structure feature of an FTIR spectrum can be retained effectively in the resolution-enhancement iterations because of the robust TV-norm.
- 2) An alternating minimization algorithm that is combined with the split Bregman iteration (SBI) method is introduced to optimize the developed FTIR spectral resolution-enhancement model. The optimization algorithm can converge effectively and has been proven in real spectral experiments.
- 3) The proposed approach obtains better performance with fewer artifacts than the state-of-the-art methods. This approach can be applied to the other robot vision imaging systems. The high-resolution IR spectrum can promote the recognition rate in the robot IR vision sensing in the intelligent system.

The rest of this article is organized as follows. Section II presents the developed resolution-enhancement model for the industrial robot IR sensing. The optimization algorithm by alternating minimization is demonstrated in Section III. Section IV provides the qualitative and quantitative experimental results and discussion on the synthesis and real FTIR spectra. The recognition methods that incorporate the resolution-enhancement algorithms are also verified. Section V concludes this article.

II. RFSIE MODEL

A. Observation Model

Resolution-enhancement technique is a fundamental problem in the robot vision [52], [53]. The latent FTIR spectrum \mathbf{x} is degraded by band overlap due to the spectrometer imaging environment change (pressure and temperature) and contaminated by the Poisson noises $\text{Pois}(\bullet)$. Thus, the FTIR imaging process can be formulated as [41], [54]

$$\mathbf{g}(v) = \text{Pois}(\mathbf{x}(v) \otimes \mathbf{k}(v)) \quad (1)$$

where $\mathbf{x}(v)$ and $\mathbf{g}(v)$ denote the high-resolution spectrum and the observed FTIR spectrum (raw data), respectively. Here, $\mathbf{k}(v)$ respects the kernel function by determining the overlap degree in the raw FTIR spectrum. \otimes denotes the convolution operation between the high-resolution spectrum and the kernel function.

Given that $\mathbf{x}(v)$ and $\mathbf{k}(v)$ are unknown (1) and cannot be estimated precisely with the Poisson noises. Thus, a classical MAP theory is adopted, in which the latent spectrum $\mathbf{x}(v)$ and kernel function $\mathbf{k}(v)$ can be calculated by maximizing *a posteriori* distribution by Bayes' rule

$$p(\mathbf{x}, \mathbf{k} | \mathbf{g}) = p(\mathbf{g} | \mathbf{x}, \mathbf{k}) p(\mathbf{x}) p(\mathbf{k}) \quad (2)$$

where $p(\mathbf{x}, \mathbf{k} | \mathbf{g})$ is the posterior probability distribution. After the logarithmic transformation, we have

$$\begin{aligned} J(\mathbf{x}, \mathbf{k}) &= -\log(p(\mathbf{x}, \mathbf{k} | \mathbf{g})) \\ &= -\log(p(\mathbf{g} | \mathbf{x}, \mathbf{k})) - \log(p(\mathbf{x})) - \log(p(\mathbf{k})). \end{aligned} \quad (3)$$

When the high-resolution IR spectrum is corrupted by the Poisson noises, each spectral intensity value in the observed spectrum $\mathbf{g}(v)$ can be considered a random variable that obeys an independent Poisson distribution. Thus, the likelihood probability can be presented as

$$p(\mathbf{g}|\mathbf{x}, \mathbf{k}) = \prod_v \frac{(\mathbf{x} \otimes \mathbf{k})_v^{\mathbf{g}_v}}{\mathbf{g}_v!} \exp \{-\mathbf{x} \otimes \mathbf{k}\} \quad (4)$$

where L denotes the size of the FTIR spectrum.

The first term in (3) can be rewritten through the following formula derivation:

$$\begin{aligned} -\log(p(\mathbf{g}|\mathbf{x}, \mathbf{k})) &= -\sum_v \log \left(\frac{(\mathbf{x} \otimes \mathbf{k})_v^{\mathbf{g}_v}}{\mathbf{g}_v!} \exp \{-\mathbf{x} \otimes \mathbf{k}\} \right) \\ &= -\sum_v (\mathbf{g}_v \log (\mathbf{x} \otimes \mathbf{k})_v - \log (\mathbf{g}_v!) - (\mathbf{x} \otimes \mathbf{k})_v) \\ &= \sum_v ((\mathbf{x} \otimes \mathbf{k})_v - \mathbf{g}_v \log (\mathbf{x} \otimes \mathbf{k})_v) + \sum_v \log (\mathbf{g}_v!). \end{aligned} \quad (5)$$

The last term $\sum_v \log (\mathbf{g}_v!)$ in (5) is a constant term. Thus, (5) can be formulated as

$$-\log(p(\mathbf{g}|\mathbf{x}, \mathbf{k})) \propto \sum_v ((\mathbf{x} \otimes \mathbf{k})_v - \mathbf{g}_v \log (\mathbf{x} \otimes \mathbf{k})_v). \quad (6)$$

B. SSIP Prior for High-Resolution Imaging Spectrum

The second density function in (3) stands for the FTIR imaging spectrum prior that constrains the smoothness in the IR spectral lines. This function usually includes the Gaussian–Markov and Laplacian–Markov prior [see Fig. 3(a)]. The form of the Markov prior is generally defined as

$$p(\mathbf{x}) = \frac{1}{Q_1} \exp \left\{ -\frac{\lambda_1}{2} \rho(|\nabla \mathbf{x}(v)|) \right\} \quad (7)$$

where Q_1 is a constant parameter. The quantity $|\nabla \mathbf{x}(v)|$, which is a spatial activity measure to the spectral wave number, is formed by the first-order difference $\nabla \mathbf{x}(v) = (\mathbf{x}(v+1) + \mathbf{x}(v-1) - 2\mathbf{x}(v))/4$. When the potential function $\rho(\bullet)$ is a linear function, the corresponding prior is regarded as Laplacian–Markov (or TV), i.e.,

$$\rho(t) = \|t\|_{TV}. \quad (8)$$

The use of the Laplacian–Markov prior is advantageous because some high-frequency components (e.g., Poisson noises) in the FTIR spectrum can be suppressed. Thus, a new spectral structure information-preserving (SSIP) prior is constructed in this article. The potential function $\rho(\bullet)$ is defined as the difference formulation in the SSIP and Laplacian–Markov priors. The potential function in the SSIP prior is constructed as

$$\rho(t) = \exp[-\theta|t|^2] \times \|t\|_{TV} \quad (9)$$

where θ is a constant parameter that can separate the plain area, noise, and structure areas, as shown in Fig. 2. The Laplacian–Markov prior is a special situation of the SSIP prior if θ is set

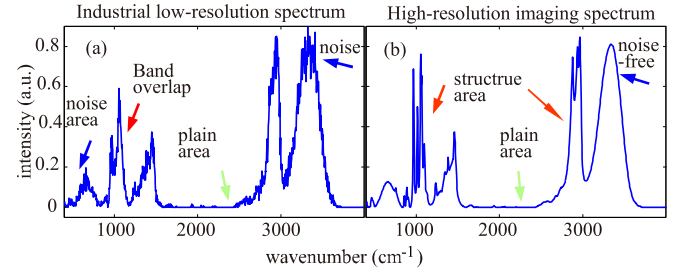


Fig. 2. Comparison of low- and high-resolution IR spectrum data with the same industrial material. IR spectrum measured by (a) industrial spectrometer imaging sensing instrument and (b) high-resolution IR imaging spectrometer instrument. The red, green, and blue arrows indicate the structure, plain, and noise areas, respectively.

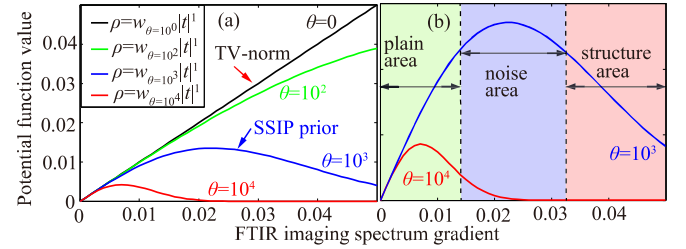


Fig. 3. Comparison between the traditional TV-norm and the proposed SSIP prior. (a) Blue line denotes the SSIP prior. (b) SSIP prior can distinguish the plain, noise, and structure areas in the IR imaging spectrum (see Fig. 2).

as 0. The expression $\exp[-\theta|\nabla \mathbf{x}|^2]$ is a monotonic decreasing function and is denoted as w_{SSIP} .

For plain area points $\|\nabla \mathbf{x}\|_{TV} \in [0, 0.015]$, gradient value is very small. Moreover, w_{SSIP} tends to 1, which indicates that a tiny TV constraint is applied to the plain area. For the noise area points $\|\nabla \mathbf{x}\|_{TV} \in [0.015, 0.032]$, $\|\nabla \mathbf{x}\|_{TV}$ and w_{SSIP} are in the middle range but achieves the largest smoothing strength. For structure areas $\|\nabla \mathbf{x}\|_{TV} \in [0.032, 0.05]$, w_{SSIP} is tiny and approaches to 0. Thus, the TV constraint is decreased. Accordingly, the spectral bands and structure are preserved effectively. Ultimately, the constructed SSIP prior can distinguish three different areas in the IR spectrum.

C. Flexible TV-Norm-Based Resolution-Enhancement Model

For the kernel function, we design the prior probability depending on the requirement of the spectral spatial smoothness. The gradient information is used to control the spectral line smoothness. Without any prior knowledge on the kernel function, the shape is approximately Gaussian. In this article, the Gaussian distribution is introduced to model the kernel function. The spectral gradient prior probability is

$$p(\mathbf{k}) = \frac{1}{Q_2} \exp \left\{ -\frac{\lambda_2}{2} \|\nabla \mathbf{k}\|^2 \right\} \quad (10)$$

where λ_2 is a positive weighted parameter that can control the smoothing strength.

Q_1 and Q_2 can be safely dropped after some manipulation by substituting (6), (9), and (10) into (3), and the posterior probability density function can be written by three probability functions. The MAP-based estimation model (3) can equal as the minimization of the cost functional, i.e.,

$$\langle \mathbf{x}, \mathbf{k} \rangle = \operatorname{argmin}[J(\mathbf{x}, \mathbf{k})] \quad (11)$$

where

$$J(\mathbf{x}, \mathbf{k}) = \sum_v^L [\mathbf{x} \otimes \mathbf{k} - \mathbf{g} \log(\mathbf{x} \otimes \mathbf{k})] + \lambda_1 w_{\text{SSIP}} \|\nabla \mathbf{x}\|_{\text{TV}} + \lambda_2 \|\nabla \mathbf{k}\|^2 \quad (12)$$

and λ_1 and λ_2 are the regularization parameters. Three terms in the developed model (12) are explained in detail as follows.

- 1) The first term represents the fidelity term of the IR spectral data, namely, the resolution-enhancement result should be satisfied with the Poisson noises observed in (1).
- 2) The second term enforces the SSIP constraint on the smoothness of the FTIR spectrum because the SSIP function can separate three kinds of spectral areas (plain, noise, and structure areas). In other words, the proposed potential function can adaptively tune the noise suppression strength with the aid of the spectral gradient feature.
- 3) The third term constrains the L_2 -norm on the kernel function intensity to remove the random noises and save the kernel function details.

In summary, this article aims to remove the random noise of the IR spectrum while the plain and structure areas of the latent spectrum as the observed one are retained. Meanwhile, the kernel function should keep the smoothness. The proposed method is named as the robust FTIR spectral imaging enhancement with a TV constraint regularization (robust FTIR spectral imaging enhancement (RFISE) hereinafter) in the industrial robot vision sensing.

III. OPTIMIZATION OF THE RFISE MODEL

Many algorithms are used to minimize the aforementioned model in (12). In this article, we utilize the alternating minimization algorithm combined with the SBI to estimate the latent FTIR spectrum. The details are presented as follows:

A. Updating the Latent Spectrum $\mathbf{x}(v)$

With a fixed kernel function $\mathbf{k}(v)$, the original model (12) can be equal to the simplified model, i.e.,

$$J(\mathbf{x}) = \sum_v^L [-\mathbf{g} \log(\mathbf{x} \otimes \mathbf{k}) + \mathbf{x} \otimes \mathbf{k}] + \lambda_1 w_{\text{SSIP}} \|\nabla \mathbf{x}\|_{\text{TV}}. \quad (13)$$

Minimizing this subproblem is difficult because the term $\|\nabla \mathbf{x}\|_{\text{TV}}$ is nonsmooth and nonconvex. Several auxiliary variables are introduced in the Bregman iterations to convert (13) into an unconstrained problem. Then, the problem is equivalent to the

optimization model, i.e.,

$$J(\mathbf{x}) = \sum_v^L [\mathbf{b}_1 - \mathbf{g} \log(\mathbf{b}_1)] + \lambda_1 w_{\text{SSIP}} \|\mathbf{b}_2\|_{\text{TV}} \quad \text{such that } \mathbf{b}_1 = \mathbf{x} \otimes \mathbf{k}, \mathbf{b}_2 = \nabla \mathbf{x}. \quad (14)$$

With the Bregman variables \mathbf{b}_1 and \mathbf{b}_2 , (14) can be transformed as the unconstrained model, i.e.,

$$J(\mathbf{x}) = \sum_v^L [\mathbf{b}_1 - \mathbf{g} \log(\mathbf{b}_1)] + \lambda_1 w_{\text{SSIP}} \|\mathbf{b}_2\|_{\text{TV}} + \frac{1}{2\alpha} \{ \|\mathbf{d}_1 + \mathbf{x} \otimes \mathbf{k} - \mathbf{b}_1\|^2 + \|\mathbf{d}_2 + \nabla \mathbf{x} - \mathbf{b}_2\|^2 \} \quad (15)$$

where α denotes the Bregman parameter. The optimization of (15) can be converted into three subproblems, namely

$$\begin{cases} \mathbf{x}^{n+1} = \arg \min_{\mathbf{x}} \frac{1}{2\alpha} \{ \|\mathbf{d}_1^n + \mathbf{x} \otimes \mathbf{k} - \mathbf{b}_1^n\|^2 + \|\mathbf{d}_2^n + \nabla \mathbf{x} - \mathbf{b}_2^n\|^2 \} \\ \mathbf{b}_1^{n+1} = \arg \min_{\mathbf{b}_1} \sum_v^L [\mathbf{b}_1 - \mathbf{g} \log(\mathbf{b}_1)] + \frac{1}{2\alpha} \|\mathbf{b}_1^n + \mathbf{x}^{n+1} \otimes \mathbf{k} - \mathbf{d}_1\|^2 \\ \mathbf{b}_2^{n+1} = \arg \min_{\mathbf{b}_2} \lambda_1 w_{\text{SSIP}} \|\mathbf{b}_2\| + \frac{1}{2\alpha} \|\mathbf{d}_2 + \nabla \mathbf{x} - \mathbf{b}_2\|^2 \\ \mathbf{d}_1^{n+1} = \mathbf{d}_1^n + (\mathbf{x}^{n+1} \otimes \mathbf{k} - \mathbf{b}_1^{n+1}) \\ \mathbf{d}_2^{n+1} = \mathbf{d}_2^n + (\nabla \mathbf{x}^{n+1} - \mathbf{b}_2^{n+1}) \end{cases} \quad (16)$$

where n is the iteration number. In (16), the first \mathbf{x} -subproblem can be optimized by the following equation:

$$(\mathbf{k}^T \otimes \mathbf{k} + 2I)\mathbf{x}^{n+1} = \mathbf{k}^T \otimes (\mathbf{d}_1^n - \mathbf{b}_1^n) + \nabla^T (\mathbf{d}_2^n - \mathbf{b}_2^n). \quad (17)$$

Equation (17) has a closed-form solution, which can be accelerated using the fast Fourier transform (FFT). This solution can be written as follows:

$$\mathbf{x}^{n+1} = \text{ifft} \left(\frac{\text{fft}(\mathbf{k}^T \otimes (\mathbf{b}_1^n - \mathbf{d}_1^n)) + \text{fft}(\nabla^T (\mathbf{b}_2^n - \mathbf{d}_2^n))}{\text{fft}(\mathbf{k}^T \otimes \mathbf{k}) + 2I} \right) \quad (18)$$

where T denotes the adjoint operation, \mathbf{I} represents the identity matrix, and $\text{fft}(\bullet)$ and $\text{ifft}(\bullet)$ are the FFT and inverse FFT, respectively.

The \mathbf{b}_1 -related subproblem in (16) can be optimized effectively as follows:

$$\mathbf{b}_1^{n+1} = \frac{1}{2} \left(\eta^n + \sqrt{(\eta^n)^2 + 4\lambda_1 \mathbf{g}} \right) \quad (19)$$

where $\eta^n = \mathbf{d}_1^{n+1} + \mathbf{k} \otimes \mathbf{g} - \lambda_1$. Similarly, \mathbf{b}_2^{n+1} can also be updated as follows:

$$\mathbf{b}_2^{n+1} = \max \{ \|\nabla \mathbf{x}^{n+1} + \mathbf{d}_2^{n+1}\| \lambda_1 \alpha * w_{\text{SSIP}}, 0 \} \times \frac{\nabla \mathbf{x}^{n+1} + \mathbf{d}_2^n}{\|\nabla \mathbf{x}^{n+1} + \mathbf{d}_2^n\|_2}. \quad (20)$$

Algorithm 1: An FTIR Imaging Spectrum Resolution-Enhancement Algorithm for the Robot IR Vision Sensing in the Intelligent System.

Input: The observed FTIR spectrum $\mathbf{x}(v)$,
 Initialization: $\mathbf{x}^0 = \mathbf{g}$, $\mathbf{k} = \mathbf{G}_{\sigma=1}$ (standard deviation value $\sigma = 1 \text{ cm}^{-1}$), $\mathbf{d}_1 = \mathbf{d}_2 = \mathbf{b}_1 = \mathbf{b}_2 = 0$, set parameters λ_1 and λ_2 ,
 1: **while** stopping criterions are not satisfied **do**
 % Updating procedure for the latent spectrum \mathbf{x}^k
 2: **Step 1:** Solve $\mathbf{x}(v)$ subproblem using (17);
 3: **Step 2:** Update the \mathbf{b}_1 -subproblem using (19);
 4: **Step 3:** Update the \mathbf{b}_2 -subproblem using (20);
 % Updating procedure for the kernel function \mathbf{k}^n
 5: **Step 4:** Solve $\mathbf{k}(v)$ subproblem by (22) and (23);
 % Updating the iteration numbers
 6: **Step 5:** $n = n + 1$.
 7: **end while**
Output: the high-resolution FTIR imaging sensing spectrum $\mathbf{x}(v)$.

B. Updating the Kernel Function $\mathbf{k}(v)$

With the fixed FTIR spectrum \mathbf{x}^{n+1} , the kernel function can be updated as

$$J(\mathbf{x}, \mathbf{k}) = \sum_v^L [\mathbf{x} \otimes \mathbf{k} - \mathbf{g} \log(\mathbf{x} \otimes \mathbf{k})] + \lambda_2 \|\nabla \mathbf{k}\|^2. \quad (21)$$

The iteration of the kernel function \mathbf{k} is formulated as

$$\mathbf{k}^{n+1} = \mathbf{k}^n \left\{ \mathbf{x}^{n+1}(-v) \otimes \left[\frac{\mathbf{g}}{\mathbf{x}^{n+1} \otimes \mathbf{k}^n} \right] \right\} \times \frac{1}{\{1 - \lambda_2 \nabla^2 \mathbf{x}\}} \quad (22)$$

and

$$\mathbf{k}^{n+1} = \frac{\mathbf{k}^{n+1}}{\sum_v^L (\mathbf{k}^{n+1})_v}. \quad (23)$$

C. Numerical Algorithm and Details

The convergence of the optimization algorithm is defined as two consecutive iterations, namely, the IR spectrum $\mathbf{x}(v)$ and the kernel function $\mathbf{k}(v)$ adjustment, which are less than the preset constant values $\|\mathbf{k}^{n+1} - \mathbf{k}^n\| / \|\mathbf{k}^n\| < d_1$ and $\|\mathbf{x}^{n+1} - \mathbf{x}^n\| / \|\mathbf{x}^n\| < d_2$. The stopping criterion values are preset between 10^{-9} and 10^{-7} . In the sequel, the intensity of all the IR spectra is normalized to the interval $[0, 1]$. In consideration of all the above-mentioned factors, the complete optimization process for the robust TV-norm smoothness constraint with the SBI can be summarized in Algorithm 1.

IV. EXPERIMENTS AND DISCUSSION

We conduct the simulation and real IR spectrum resolution-enhancement experiments on different industrial grasping materials to compare our RFISE model with the previous approaches for illustrating its effectiveness.

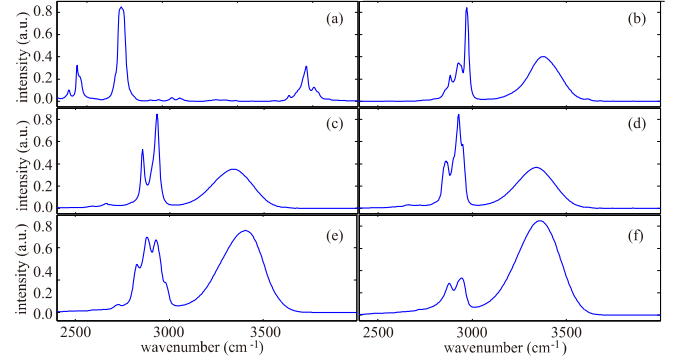


Fig. 4. Six test FTIR imaging spectra for simulated experiments. Industrial materials of (a) methyl formate, (b) tert-amyl alcohol, (c) monomethyl ether, (d) ethylene glycol, (e) cyclohexanol, and (f) 3-methylcyclohexanol. These industrial materials are often used in the manufacturing production. Their IR imaging spectra can be captured by the industrial robot vision system.

A. Experimental Setup

The FTIR spectrum used in our simulated experiments is shown in Fig. 4. All the results of the developed approach are compared with those of the several state-of-the-art methods, such as the spectral imaging recovery with the Wiener estimation method (SIRWE) [28], the IR spectral enhancement based on the fuzzy radial basis function neural network (ISENN) [1], and the spectral-resolution enhancement technology with the modified φ HS regularization (SRET) [29]. The ISENN and SRET method implementations are kindly provided by Prof. Victor and Zhu, respectively.

We keep the track of the normalized mean square error (NMSE) in every iteration to examine the convergence. A quantitative evaluation is conducted for the recovered spectra with three metrics, namely, a self-weighted correlation coefficient (WCC) [55], a ratio of the full width at half-maximum (R_{FWHM}) [41], and a ratio of the noise suppression (R_{NS})

$$R_{FWHM} = \frac{1}{L} \sum_v^L \text{FWHM}_g^{(v)} / \text{FWHM}_x^{(v)} \quad (24)$$

$$R_{NS} = \sum |\nabla \mathbf{g}| / |\nabla \mathbf{x}| \quad (25)$$

where $\text{FWHM}_g^{(v)}$ and $\text{FWHM}_x^{(v)}$ denote the bandwidth for spectra \mathbf{g} and \mathbf{x} , respectively. R_{NS} represents the ratio of the TV of \mathbf{g} to that of the recovered spectrum \mathbf{x} and serves as the noise attenuation measure. The reference spectrum \mathbf{x} is required in the NMSE. Thus, the NMSE works robustly in simulated experiments. R_{FWHM} and R_{NS} , which require no-reference measure for the FTIR spectra, are suitable for experiments with the real FTIR spectra. Furthermore, R_{FWHM} and R_{NS} can reflect the band split overlap and noise reduction. Large values of the two metrics indicate that the recovered spectra results are good.

B. Simulated Experimental Results

The simulated experiments with the six Poisson noise-contaminated spectra (see Fig. 4) are conducted to verify the

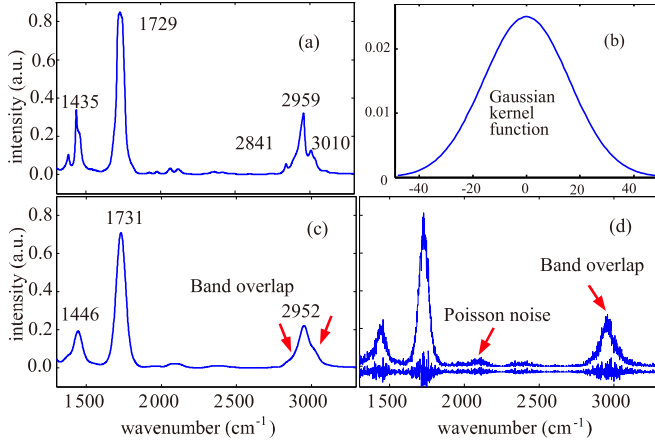


Fig. 5. IR imaging spectrum data simulation experiment. (a) IR spectrum of methyl formate from 1300 to 3300 cm^{-1} . (b) Gaussian-shape kernel function with $\sigma = 12 \text{ cm}^{-1}$. (c) Overlap spectrum. (d) Contaminated by the Poisson noises (SNR = 200).

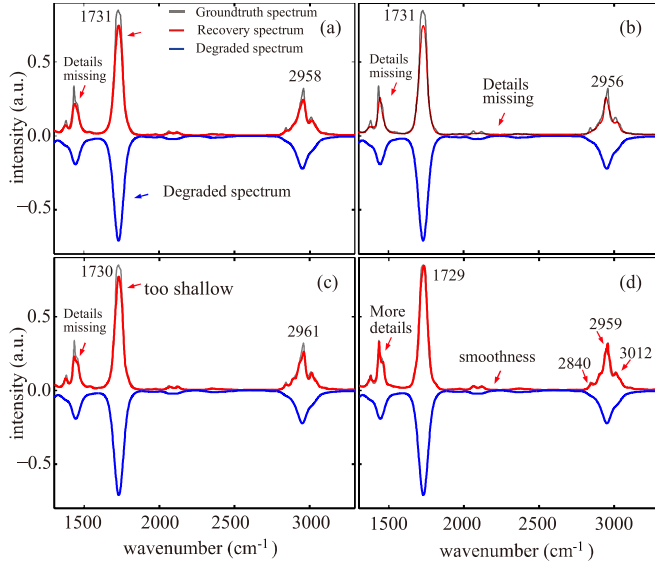


Fig. 6. Simulation experiments in noise-free case. (a) SIRWE model [28]. (b) ISENN model [1]. (c) SRET [29]. (d) Proposed RFISE method. The band height and peak positions are important features in the robot IR vision sensing.

robustness of our model. The spectra are selected from the spectral dataset of Bruker Optics Incorporation. The Gaussian function is added to degrade these spectra by the standard variance of 12 cm^{-1} [see Fig. 5(b)]. After the degradation, the spectra show more smoothness, lower resolution, and lower and wider bands than before [see Fig. 5(c)]. For instance, the original peaks of 2841, 2959, and 3010 cm^{-1} in Fig. 5(a) are difficult to differentiate. Fig. 5(d) shows that the overlapped spectrum is contaminated by the Poisson noises. The three state-of-the-art models, namely, the SIRWE, ISENN, and SRET methods, are adopted for comparison.

Fig. 6(a)–(c) shows the restoration results for the simulated cases by the ISENN, SRET, and RFISE methods. We choose

TABLE I
BAND DISTORTIONS OF THE FTIR SPECTRA ENHANCED BY THE SIRWE, ISENN, SRET, AND RFISE METHODS IN Fig. 6

Band Param.	Methods	1435	1729	2841	2959	3010	RMSE
Position	SIRWE	0	+2	--	-1	+3	0.1868
	ISENN	+2	+2	--	-3	+3	0.1709
	SRET	+1	+1	-1	+2	-2	0.1571
	RFISE	0	0	+1	0	+2	0.0980
Height	SIRWE	-0.214	-0.185	--	-0.125	-0.075	1.6432
	ISENN	-0.182	-0.178	--	-0.143	-0.112	1.5166
	SRET	-0.201	-0.151	-0.015	-0.121	-0.018	1.3038
	RFISE	-0.010	-0.012	-0.013	-0.102	-0.016	0.8371

$\lambda_1 = 0.05$, $\lambda_2 = 300$, and 20 iterations. Comparison between Fig. 6(d) with 6(a)–(c) reveals that an RFISE can preserve the spectral structure while the noises are decreased effectively. The gray lines denote the groundtruth spectrum. Fig. 6(a)–(c) shows that the peaks at 1731 cm^{-1} are lower than the groundtruth one. However, Fig. 6(d) displays that the recovered peak is close to the groundtruth. The degraded peak at 1446 cm^{-1} [see Fig. 5(c)] is reconstructed very well in Fig. 6(d). Other results have some missing details.

Peak distortions are investigated for comparing the resolution-enhancement performance of the four approaches. In the noncontaminated spectrum [see Fig. 5(a)], five peaks at 1435, 1729, 2841, 2959, and 3010 cm^{-1} are selected for comparison. Table I lists the distortions of these peaks in terms of position and height between the resolution-enhancement result (see red lines in Fig. 6) and the noncontaminated spectrum (see gray lines in Fig. 6). These distortions of the RMSE values are computed. For the RMSE, the distortions in peak position and height by the RFISE model show less in value than those by the SIRWE, ISENN, and SRET models. In particular, the recovered spectrum in Fig. 6(d) is closest to the groundtruth. Therefore, the RFISE method can enhance the spectral resolution effectively when the spectral structure details are produced.

C. Performance of Noise Suppression

The noisy spectrum is simulated with noise level SNR = 200 [see Fig. 5(d)] for investigating the robustness of the spectral resolution-enhancement approaches to the Poisson noises. Fig. 7(a)–(d) shows the resolution-enhanced results by SIRWE, ISENN, SRET, and RFISE, respectively. Overall, the spectral noises (blue lines) are suppressed effectively and reconstructed as red lines in Fig. 7. Specifically, the resolution-enhanced spectrum in Fig. 7(a) presents less split and more residual noises than those in other figures. The ringing artifact (third red arrow) can be observed in Fig. 7(b). The fake peaks are indicated by the fourth red arrow. The spectral structures are not recovered effectively [see Fig. 7(b) and (c)] and have missing details (the peak at 1435 cm^{-1}). As shown in Fig. 7(d), the proposed method recovers a very sharp spectrum, which is very similar to the groundtruth spectrum. The reason is the proposed SSIP prior can distinguish the structure, plain, and

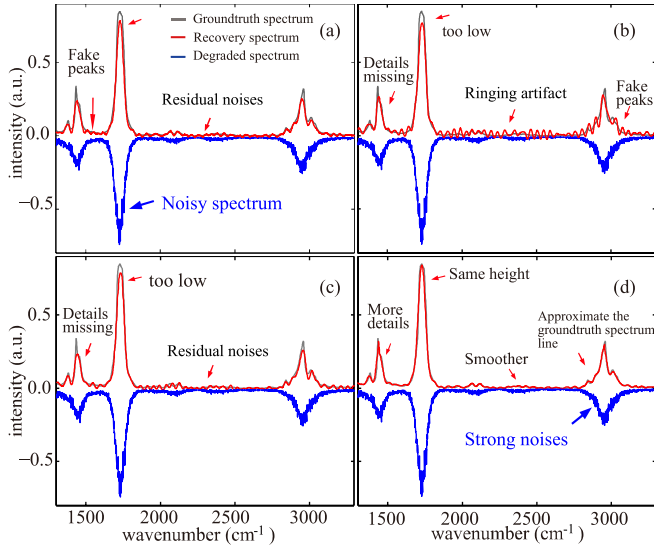


Fig. 7. Noise suppression experiments for the IR imaging spectrum (SNR = 200). (a) SIRWE [28] model. (b) ISENN model [1]. (c) SRET [29] model. (d) Our RFISE model.

TABLE II

NMSE, WCC, R_{FWHM} , AND R_{NS} OF ORIGINAL SPECTRUM AND THE BEST ENHANCEMENT SPECTRUM (WITH THE LOWEST NMSE BY DIFFERENT ALGORITHMS) FOR NOISE-FREE AND SNR = 200 (IN BRACKETS) CASES

Industrial materials	Merits	Spectral resolution-enhancement algorithms by			
		SIRWE [27]	ISENN [1]	SRET [28]	RFISE
Methyl formate	NMSE	0.0352 (0.0382)	0.0313 (0.0331)	0.0256 (0.0278)	0.0225 (0.0246)
	WCC	0.9889 (0.9881)	0.9929 (0.9917)	0.9935 (0.9926)	0.9948 (0.9942)
	R_{FWHM}	2.16 (1.95)	2.66 (2.31)	3.35 (3.08)	3.89 (3.65)
	R_{NS}	1.92 (1.81)	2.36 (2.02)	2.90 (2.67)	3.16 (2.98)
		0.0406 (0.0421)	0.0375 (0.0388)	0.0261 (0.0272)	0.0231 (0.0242)
Tert-a myl alcohol	WCC	0.9876 (0.9869)	0.9902 (0.9886)	0.9932 (0.9921)	0.9956 (0.9941)
	R_{FWHM}	1.95 (1.72)	2.63 (2.38)	2.99 (2.75)	3.27 (2.99)
	R_{NS}	1.42 (1.35)	1.89 (1.76)	2.02 (1.89)	2.47 (2.25)

Small values of the NMSE indicate that the recovered spectrum has high quality. Other merits are the opposite.

noise areas in the degraded spectrum. However, the compared methods only consider the noise suppression ability. Table II reports the resolution-enhancement results by various compared approaches on the simulated IR spectrum. As given in the table, our approach achieves better performance than the previous articles [56].

D. Real Experimental Results

Our method is applied on the real FTIR spectra. The FTIR imaging spectra often suffer from the contamination of the Poisson noises because of the photon-limited detection in the industrial robot vision system. The six FTIR spectra obtained

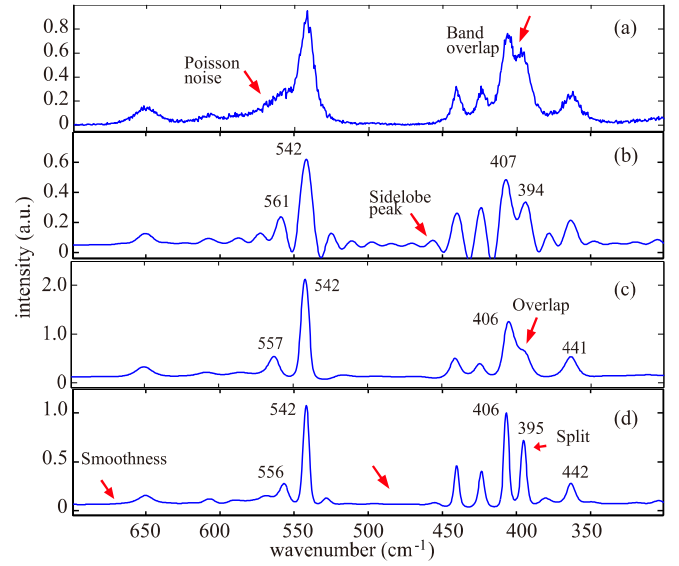


Fig. 8. Real FTIR imaging spectrum experiment of industrial material of Cr:LisAF crystal. (a) FTIR spectrum from 10 to 700 cm^{-1} . (b) ISENN result [1]. (c) SRET result [29]. (d) Proposed RFISE.

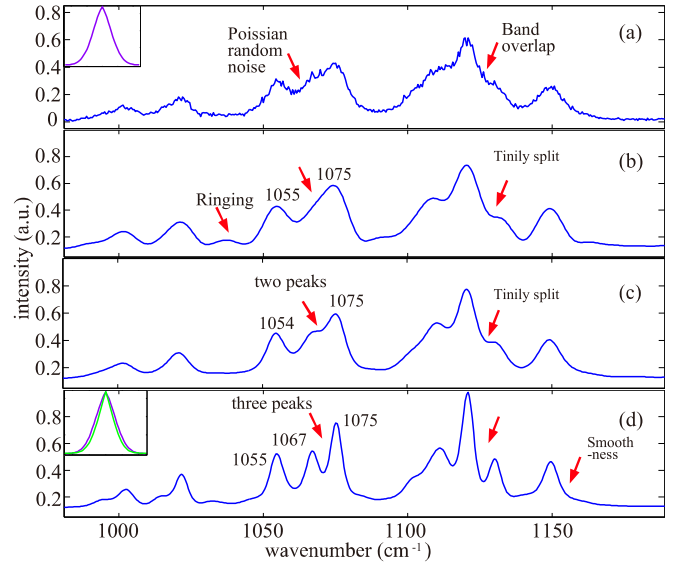


Fig. 9. Real FTIR spectrum enhancement experiments. (a) Raw data of an FTIR spectrum ((D+)-glucopyranose) [57]. (b) ISENN result [1]. (c) SRET result [29]. (d) Proposed RFISE result.

from [57] are tested. To save space, only two of them are illustrated. For an RFISE, we set $\lambda_1 = 0.05$ and $\lambda_2 = 250$ and initialize the kernel function by a Gaussian function with the standard deviation $\sigma = 1 \text{ cm}^{-1}$. Fig. 8(a) shows a 400 cm^{-1} length spectrum of Cr:LisAF crystal ranging from 700 to 300 cm^{-1} . The overlap bands in Fig. 8(a) are recovered into two bands at 407 and 394 cm^{-1} in Fig. 8(b) (ISENN method) and 406 and 395 cm^{-1} in Fig. 8(d) (RFISE method). The band in Fig. 8(c) is insufficiently split. With regard to the noise suppression, Fig. 8(d) shows the smoothest spectral line.

TABLE III

R_{FWHM} AND R_{NS} (IN BRACKET) VALUES OF THE DIFFERENT RESOLUTION-ENHANCEMENT ALGORITHMS ON THE REAL FTIR SPECTRA

Spectral lines	SIRWE [27]	ISENN [1]	SRET [28]	RFISE
IR 1	2.78 (1.86)	3.01 (2.01)	3.42 (2.28)	3.89 (2.56)
IR 2	2.81 (1.91)	3.22 (2.16)	3.63 (2.47)	4.05 (2.73)
IR 3	3.28 (2.11)	3.75 (2.32)	4.16 (2.65)	4.56 (2.98)
IR 4	2.64 (1.81)	2.85 (2.03)	3.28 (2.21)	3.73 (2.48)
IR 5	3.19 (1.92)	3.66 (2.01)	3.92 (2.12)	3.35 (2.34)
IR 6	2.91 (2.09)	3.28 (2.31)	3.69 (2.61)	4.12 (2.81)

Large values of R_{FWHM} and R_{NS} indicate that the spectral quality is good.

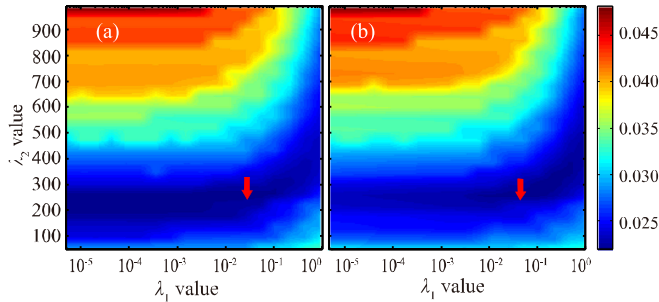


Fig. 10. NMSE versus regularization parameters λ_1 and λ_2 of an RFISE method for the FTIR spectrum of industrial material (methyl formate). (a) Noise-free case. (b) Noisy case (SNR = 200).

Fig. 9(a) shows a (D+)-glucopyranose FTIR spectrum with a length of 690 [57] from 950 to 1200 cm^{-1} . Fig. 9(b)–(d) illustrates the spectral resolution-enhancement results of the ISENN, SRET, and RFISE methods, respectively. The Poisson noises are effectively removed by all the compared methods. The overlap band (left red arrow) is divided into two peaks at 1067 and 1075 cm^{-1} in Fig. 9(d). However, this band is still overlap in Fig. 9(b) and (c). Only two band features can be extracted in Fig. 9(c), whereas three bands can be extracted in Fig. 9(d). The spectral resolution and the relative intensity distortion are effectively recovered. Table III illustrates the R_{FWHM} and R_{NS} values for the six FTIR spectra. All the spectral resolution-enhancement algorithms increase R_{FWHM} and R_{NS} to some extent, whereas our approaches achieve the best result.

E. Discussion

Regularization parameter determination: In the proposed (12), λ_1 and λ_2 aim to balance the first term and two regularization terms. We carry out two experiments on the FTIR imaging spectra (see Fig. 10) to analyze the influence of the two parameters on the resolution-enhanced results for selecting the suitable regularization parameters. Specifically, λ_1 is ranged from 10^{-5} to 1, and λ_2 is ranged from 1 to 999. In the

TABLE IV

COMPUTATION TIMES (IN SECONDS) OF THE DIFFERENT RESOLUTION-ENHANCEMENT ALGORITHMS IN THREE SPECTRAL LENGTHS FOR THE SIRWE, ISENN, SRET, AND RFISE METHODS

Length	SIRWE [27]	ISENN [1]	SRET [28]	RFISE
400 cm^{-1}	3.592	0.395	1.364	0.035
690 cm^{-1}	6.587	0.831	2.183	0.097
2000 cm^{-1}	12.516	1.351	3.954	0.212

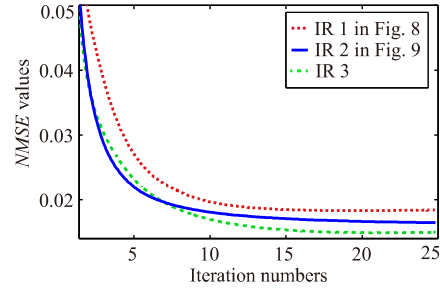


Fig. 11. NMSE values along with the iteration number of the proposed two models for the FTIR spectrum.

experiments, the NMSE values are introduced to evaluate the effect of the regularization parameters. For the noise-free and noisy cases, the best ranges for the two parameters are $\lambda_1 \in [0.025, 0.035]$ and $\lambda_2 \in [200, 300]$. Thus, the regularization parameters are set to the default values of $\lambda_1 = 0.03$ and $\lambda_2 = 250$.

Running time: Our algorithm obtains the high-resolution recovered spectra via (12), which is accelerated by the FFT. The optimization equations (18)–(20) are optimized with the shrinkage operation parallelly. This operation is very fast and needs only several step computations for each element. Thus, all the rapid calculations enable a real-time operation of the proposed model. We compare the running time of the several state-of-the-art FTIR spectrum resolution-enhancement algorithms, as given in Table IV. The running time lasts around 0.035 and 0.097 s for processing the FTIR spectra, as shown in Figs. 8 and 9, respectively. These processing times are faster than those of the SRET method (1.364 and 2.183 s). The RFISE approach is very rapid and can be further accelerated in the hardware implementation.

Convergence: The convergence property of our method is tested. Fig. 11 presents the NMSE and the number of iterations of the three FTIR spectra of industrial materials by our approach. The relationship between the NMSE values and the iteration numbers is clearly demonstrated. Specifically, the NMSE decreases dramatically as the iteration number increases. This result verifies the convergence (after only 15 iterations) of the alternative minimization algorithm for optimizing the proposed approaches.

F. Application for Industrial Robot Vision Sensing

The FTIR imaging spectrum recognition provides rich material information for industrial robot vision sensing. The robot can set accurate parameters, such as grasping force and friction

TABLE V
COMPARISON RESULTS WITH CURRENT STATE-OF-THE-ART ALGORITHMS

Methods + SVM	Accuracy (%)
Without process	56.36
ISENN [1]	85.71
SRET [28]	90.42
Proposed RFISE	97.51

Organosilicon	97.22	0.00	0.00	2.65	0.00	0.13	0.00	0.00	0.00
Halomethane	0.39	95.91	0.00	0.00	1.50	0.00	2.20	0.00	0.00
Organofluoric	0.00	0.00	99.64	0.28	0.00	0.08	0.00	0.00	0.00
Cumene	1.10	0.00	2.49	94.41	0.00	0.92	0.80	0.00	0.28
Benzylacetate	0.00	0.00	0.00	0.00	100	0.00	0.00	0.00	0.00
Furfural	0.90	0.00	1.05	0.59	0.00	96.81	0.00	0.65	0.00
Nitroethane	0.00	1.40	0.00	0.00	0.00	1.00	97.35	0.00	0.25
Sulfolane	0.00	0.00	1.20	0.00	0.00	2.00	0.00	96.80	0.00
Cyclohexanol	0.00	0.00	0.00	0.00	0.80	0.00	0.20	0.00	99.00

Fig. 12. Comparison of confusion matrices with sixfold industrial materials cross validation [58] by the RFISE method.

coefficients. The FTIR spectral dataset [58] is an industrial material IR and FTIR spectral library presented by Dr. Ludmila. This dataset contains the quantitative IR (13 entries) and FTIR (two entries). This sample library collects the IR spectra for the industrial material of organosilicon, halomethane, and organofluoric compounds recorded at different pressures. All the IR imaging spectra are degraded by band overlap and random noise. Thus, the spectra are suited for the qualitative and quantitative investigations.

We examine the experimental results among the four methods on this dataset. The parameters in the state-of-the-art approaches are adjusted to the best values reported in their respective articles. The linear support vector machine classifier is used for all the comparison methods for fair comparison. Table V lists our results and those of the existing state of the arts. The proposed RFISE approach obtains a competitive result of 97.51% compared with the best result. The recognition rate of the original IR spectra without any process only equals to 56.36% (see Table V). The confusion matrices obtained by the SRET and the proposed approach are shown in Fig. 12 for examining the results further. Most of the industrial materials can be effectively classified, whereas the performance on several similar industrial materials still needs to be improved.

V. CONCLUSION

In this article, we introduced a flexible SSIP-based resolution-enhancement algorithm for a robot IR vision sensing in industrial intelligent systems. Specifically, the proposed SSIP prior is used to differentiate the various structures (i.e., plain, noise, and structure areas) in the IR imaging spectrum. Apart from using the adaptive TV-norm to characterize the spectral line

structures, we also considered a Gaussian distribution regularization to model the kernel function in the practical scenarios. An SBI-based optimization algorithm was designed to estimate the high-resolution spectrum and kernel function. The algorithm was proven to have a good convergence and stability. The IR spectral-resolution enhancement experiments showed the superior effect of our model over some state-of-the-art algorithms on visual comparison and quantitative evaluation. Experiments on the IR spectrum datasets emphasized the effectiveness of our RFISE method. Our RFISE method can be applied in solving various industrial robot vision sensing problems in industrial intelligent systems because of its fast implementation.

However, the performance of our method can still be improved. For example, the optimization of the nonconvex TV-norm model by evolutionary computation can be used to solve nonconvex issues in the industrial robot vision sensing [59]. Thus, we will consider this method in the future.

REFERENCES

- [1] S.-B. Roh, S.-K. Oh, and W. Pedrycz, "Identification of black plastics based on fuzzy RBF neural networks: Focused on data preprocessing techniques through Fourier transform infrared radiation," *IEEE Trans. Ind. Inform.*, vol. 14, no. 5, pp. 1802–1813, May 2018.
- [2] H. Zhang *et al.*, "An infrared-induced terahertz imaging modality for foreign object detection in a lightweight honeycomb composite structure," *IEEE Trans. Ind. Inform.*, vol. 14, no. 12, pp. 5629–5636, Dec. 2018.
- [3] A. L. Serrano *et al.*, "Wide-field FTIR microscopy using mid-IR pulse shaping," *Opt. Express*, vol. 23, no. 14, pp. 17815–17827, 2015.
- [4] M. J. Baker *et al.*, "Using Fourier transform IR spectroscopy to analyze biological materials," *Nature Protocols*, vol. 9, no. 8, pp. 1771–1791, 2014.
- [5] R. Sakurai, S. Yamane, and J.-H. Lee, "Restoring aspect ratio distortion of natural images with convolutional neural network," *IEEE Trans. Ind. Inform.*, vol. 15, no. 1, pp. 563–571, Jan. 2019.
- [6] S. Y. Chen, J. Zhang, H. Zhang, N. M. Kwok, and Y. F. Li, "Intelligent lighting control for vision-based robotic manipulation," *IEEE Trans. Ind. Electron.*, vol. 59, no. 8, pp. 3254–3263, Aug. 2012.
- [7] T. Liu, H. Liu, Y. Li, Z. Zhang, and S. Liu, "Efficient blind signal reconstruction with wavelet transforms regularization for educational robot infrared vision sensing," *IEEE/ASME Trans. Mechatron.*, vol. 24, no. 1, pp. 384–394, Feb. 2019.
- [8] Y. Guo, Y. F. Li, and Z. Shao, "On multi-scale self-similarities description for effective three-dimensional/six-dimensional motion trajectory recognition," *IEEE Trans. Ind. Inform.*, vol. 13, no. 6, pp. 3017–3026, Dec. 2017.
- [9] Y. Guo, Y. Li, and Z. Shao, "RRV: A spatiotemporal descriptor for rigid body motion recognition," *IEEE Trans. Cybern.*, vol. 48, no. 5, pp. 1513–1525, May 2018.
- [10] D. Su, Y.-F. Li, and H. Chen, "Towards precise gaze estimation for mobile head-mounted gaze tracking systems," *IEEE Trans. Ind. Inform.*, vol. 15, no. 5, pp. 2660–2672, May 2019.
- [11] H. Chen, Y. Li, and D. Su, "Multi-modal fusion network with multi-scale multi-path and cross-modal interactions for RGB-D salient object detection," *Pattern Recognit.*, vol. 86, pp. 376–385, 2019.
- [12] N. P. Ayerden and R. F. Wolffenbuttel, "The miniaturization of an optical absorption spectrometer for smart sensing of natural gas," *IEEE Trans. Ind. Electron.*, vol. 64, no. 12, pp. 9666–9674, Dec. 2017.
- [13] X. Dai *et al.*, "A novel image-guided FT-IR sensor using chalcogenide glass optical fibers for the detection of combustion gases," *Sensors Actuators B, Chem.*, vol. 220, pp. 414–419, 2015.
- [14] J. Ma *et al.*, "Locality preserving matching," *Int. J. Comput. Vis.*, vol. 127, no. 5, pp. 512–531, 2019.
- [15] K. Sun and W. Tao, "A center-driven image set partition algorithm for efficient structure from motion," *Inf. Sci.*, vol. 479, pp. 101–115, 2019.
- [16] I. Mukhopadhyay and B. E. Billingham, "High resolution synchrotron radiation Fourier transform infrared spectrum of the COH-bending mode in methanol-D1 (CH₂DOH)," *Infrared Phys. Technol.*, vol. 85, pp. 184–210, 2017.

- [17] H. Liu *et al.*, "Blind Poissonian reconstruction algorithm via curvelet regularization for an FTIR spectrometer," *Opt. Express*, vol. 26, no. 18, pp. 22837–22856, 2018.
- [18] T. Sun *et al.*, "Magnetic alginate microfibers as scaffolding elements for the fabrication of microvascular-like structures," *Acta Biomater.*, vol. 66, pp. 272–281, 2018.
- [19] C. J. Manning, and P. R. Griffiths, "Noise sources in step-scan FT-IR spectrometry," *Appl. Spectrosc.*, vol. 51, no. 8, pp. 1092–1101, 1997.
- [20] H. Liu *et al.*, "Joint baseline-correction and denoising for Raman spectra," *Appl. Spectrosc.*, vol. 69, no. 9, pp. 1013–1022, 2015.
- [21] H. Chen and Y. Li, "Three-stream attention-aware network for RGB-D salient object detection," *IEEE Trans. Image Process.*, vol. 28, no. 6, pp. 2825–2835, Jun. 2019.
- [22] H. Chen and Y. Li, "Progressively complementarity-aware fusion network for RGB-D salient object detection," in *Proc. IEEE/CVF Conf. Comput. Vis. Pattern Recognit.*, Salt Lake City, UT, USA, 2018, pp. 3051–3060.
- [23] H. Liu, S. Chen, and N. Kubota, "Intelligent video systems and analytics: A survey," *IEEE Trans. Ind. Inform.*, vol. 9, no. 3, pp. 1222–1233, Aug. 2013.
- [24] W. Zhang *et al.*, "Spectrum reconstruction in Fourier transform imaging spectroscopy based on high-performance parallel computing," *Appl. Opt.*, vol. 57, no. 21, pp. 5983–5991, 2018.
- [25] V. Sizikov and D. Sidorov, "Discrete spectrum reconstruction using integral approximation algorithm," *Appl. Spectrosc.*, vol. 71, no. 7, pp. 1640–1651, 2017.
- [26] T. Liu *et al.*, "FBRDLR: Fast blind reconstruction approach with dictionary learning regularization for infrared microscopy spectra," *Infrared Phys. Technol.*, vol. 90, pp. 101–109, 2018.
- [27] Q. Han *et al.*, "Simultaneous spectrum fitting and baseline correction using sparse representation," *Analyst*, vol. 142, no. 13, pp. 2460–2468, 2017.
- [28] S. Chen *et al.*, "Recovery of Raman spectra with low signal-to-noise ratio using wiener estimation," *Opt. Express*, vol. 22, no. 10, pp. 12102–12114, 2014.
- [29] H. Zhu *et al.*, "Spectral semi-blind deconvolution methods based on modified φ HS regularizations," *Opt. Laser Technol.*, vol. 110, pp. 24–29, 2019.
- [30] B. Yi *et al.*, "Deep matrix factorization with implicit feedback embedding for recommendation system," *IEEE Trans. Ind. Inform.*, vol. 15, no. 8, pp. 4591–4601, Aug. 2019.
- [31] T. Liu, Y. F. Li, H. Liu, Z. Zhang, and S. Liu, "RISIR: Rapid infrared spectral imaging restoration model for industrial material detection in intelligent video systems," *IEEE Trans. Ind. Inform.*, to be published, doi: [10.1109/TII.2019.2930463](https://doi.org/10.1109/TII.2019.2930463).
- [32] K. Kondo, Y. Ichioka, and T. Suzuki, "Image restoration by Wiener filtering in the presence of signal-dependent noise," *Appl. Opt.*, vol. 16, no. 9, pp. 2554–2558, 1977.
- [33] M. B. Slima, R. Z. Morawski, and A. Barwicz, "Kalman-filter-based algorithms of spectrophotometric data correction III. Use of splines for approximation of spectra," *IEEE Trans. Instrum. Meas.*, vol. 46, no. 3, pp. 685–689, Jun. 1997.
- [34] S. Y. Chen, "Kalman filter for robot vision: A survey," *IEEE Trans. Ind. Electron.*, vol. 59, no. 11, pp. 4409–4420, Nov. 2012.
- [35] F. Auger, M. Hilaret, J. M. Guerrero, E. Monmasson, and T. Orłowska-Kowalska, "Industrial applications of the Kalman filter: A review," *IEEE Trans. Ind. Electron.*, vol. 60, no. 12, pp. 5458–5471, Dec. 2013.
- [36] Y. Senga *et al.*, "Estimation of spectral slit width and blind deconvolution of spectroscopic data by homomorphic filtering," *Appl. Opt.*, vol. 23, no. 10, pp. 1601–1608, 1984.
- [37] V. A. Lórenz-Fonfría and E. Padrós, "The role and selection of the filter function in Fourier self-deconvolution revisited," *Appl. Spectrosc.*, vol. 63, no. 7, pp. 791–799, 2009.
- [38] P. A. Jansson, *Deconvolution: With Applications in Spectroscopy*. New York, NY, USA: Academic, 1984.
- [39] P. B. Crilly, "Increased throughput for process chromatography using constrained deconvolution," *IEEE Trans. Ind. Electron.*, vol. 39, no. 1, pp. 20–24, Feb. 1992.
- [40] S. Sarkar, P. K. Dutta, and N. C. Roy, "A blind-deconvolution approach for chromatographic and spectroscopic peak restoration," *IEEE Trans. Instrum. Meas.*, vol. 47, no. 4, pp. 941–947, Aug. 1998.
- [41] J. Kutrašnik, F. Pernu, and B. Likar, "Deconvolution in acousto-optical tunable filter spectrometry," *Appl. Spectrosc.*, vol. 64, no. 11, pp. 1265–1273, 2010.
- [42] S. Chen *et al.*, "Stepwise method based on Wiener estimation for spectral reconstruction in spectroscopic Raman imaging," *Opt. Express*, vol. 25, no. 2, pp. 1005–1018, 2017.
- [43] H. Liu *et al.*, "Blind spectral deconvolution algorithm for Raman spectrum with Poisson noise," *Photon. Res.*, vol. 2, no. 6, pp. 168–171, 2014.
- [44] H. Liu *et al.*, "Richardson-Lucy blind deconvolution of spectroscopic data with wavelet regularization," *Appl. Opt.*, vol. 54, no. 7, pp. 1770–1775, 2015.
- [45] L. Deng, H. Zhu, and G. Lu, "THz spectrum deconvolution with total variation regularization," in *Proc. 6th Int. Congr. Image Signal Process.*, Hangzhou, China, 2013, pp. 1272–1276.
- [46] H. Liu *et al.*, "Adaptive total variation-based spectral deconvolution with the split Bregman method," *Appl. Opt.*, vol. 53, no. 35, pp. 8240–8248, 2014.
- [47] H. Zhu *et al.*, "Deconvolution methods based on convex regularization for spectral resolution enhancement," *Comput. Elect. Eng.*, vol. 70, pp. 959–967, 2018.
- [48] H. Liu *et al.*, "Multi-order blind deconvolution algorithm with adaptive Tikhonov regularization for infrared spectroscopic data," *Infrared Phys. Technol.*, vol. 71, pp. 63–69, 2015.
- [49] H. Liu, L. Yan, Y. Chang, H. Fang, and T. Zhang, "Spectral deconvolution and feature extraction with robust adaptive Tikhonov regularization," *IEEE Trans. Instrum. Meas.*, vol. 62, no. 2, pp. 315–327, Feb. 2013.
- [50] Q. Liu *et al.*, "Depth IR spectroscopic data resolution improvement for antibiotics component analysis in critically ill elderly patients," *Infrared Phys. Technol.*, vol. 93, pp. 291–299, 2018.
- [51] J. Ma, J. Jiang, H. Zhou, J. Zhao, and X. Guo, "Guided locality preserving feature matching for remote sensing image registration," *IEEE Trans. Geosci. Remote Sens.*, vol. 56, no. 8, pp. 4435–4447, Aug. 2018.
- [52] H. Zhu *et al.*, "Deconvolution methods based on φ HL regularization for spectral recovery," *Appl. Opt.*, vol. 54, no. 14, pp. 4337–4344, 2015.
- [53] V. A. Lórenz-Fonfría, J. Villaverde, and E. Padrós, "Fourier deconvolution in non-self-deconvolving conditions. Effective narrowing, signal-to-noise degradation, and curve fitting," *Appl. Spectrosc.*, vol. 56, no. 2, pp. 232–242, 2002.
- [54] D. C. Fernandez *et al.*, "Infrared spectroscopic imaging for histopathologic recognition," *Nature Biotechnol.*, vol. 23, pp. 469–474, 2005.
- [55] P. R. Griffiths and L. Shao, "Self-weighted correlation coefficients and their application to measure spectral similarity," *Appl. Spectrosc.*, vol. 63, no. 8, pp. 916–919, 2009.
- [56] T. Liu, H. Liu, Z. Chen, and A. M. Lesgold, "Fast blind instrument function estimation method for industrial infrared spectrometers," *IEEE Trans. Ind. Inform.*, vol. 14, no. 12, pp. 5268–5277, Dec. 2018.
- [57] S. B. Engelson, "Infrared spectral of D(+)-cellobiose," 2019. [Online]. Available: <http://www.models.life.ku.dk/specarb>
- [58] L. Tumanova, "IR and FT-IR spectral library," 2019. [Online]. Available: https://www.acdlabs.com/resources/knowledgebase/samples_dbs/
- [59] L. Jiao *et al.*, "A novel image representation framework based on gaussian model and evolutionary optimization," *IEEE Trans. Evol. Comput.*, vol. 21, no. 2, pp. 265–280, Apr. 2017.



Tingting Liu (S'18) received the M.S. degree in computer application from the Huazhong University of Science and Technology, Wuhan, China, in 2014. She is currently working toward the Ph.D. degree in management science and engineering with Central China Normal University, Wuhan, China.

From September 2017 to September 2019, she was a visiting student with the University of Pittsburgh, Pittsburgh, PA, USA. From May 2019 to September 2019, she was a Research

Assistant with the Institute of Human-Computer Interaction, Carnegie Mellon University, Pittsburgh, PA, USA. She has authored more than 30 peer-reviewed articles in international journals from multiple domains. Her current research interests include signal processing, robot vision, educational technology, and deep learning.



Hai Liu (S'12–M'14) received the M.S. degree in applied mathematics and the Ph.D. degree in pattern recognition and artificial intelligence from the Huazhong University of Science and Technology, Wuhan, China, in 2010 and 2014, respectively.

Since June 2017, he has been an Assistant Professor with the National Engineering Research Center for E-Learning, Central China Normal University, Wuhan. He was a "Hong Kong Scholar" Postdoctoral Fellow with the Department of Mechanical Engineering, City University of Hong Kong, Kowloon, Hong Kong, where he was hosted by the Professor Y.-F. Li; he held the position for two years till March 2019. He has authored more than 60 peer-reviewed articles in international journals from multiple domains such as pattern recognition and image processing. His current research interests include big data processing, artificial intelligence, spectral analysis, optical data processing, and pattern recognition.

Dr. Liu has been frequently serving as a Reviewer for more than six international journals including the IEEE TRANSACTIONS ON INDUSTRIAL INFORMATICS, IEEE TRANSACTIONS ON CYBERNETICS, the IEEE/ASME TRANSACTIONS ON MECHATRONICS, and IEEE TRANSACTIONS ON INSTRUMENTATION AND MEASUREMENT. He is also a Communication Evaluation Expert for the National Natural Science Foundation of China.

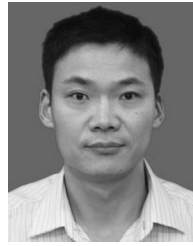


You-Fu Li (M'91–SM'01) received the B.S. and M.S. degrees in electrical engineering from the Harbin Institute of Technology, Harbin, China, and the Ph.D. degree in robotics from the Department of Engineering Science, University of Oxford, Oxford, U.K., in 1993.

From 1993 to 1995, he was a member of the Research Staff with the Department of Computer Science, University of Wales, Aberystwyth, U.K. He joined the City University of Hong Kong, Hong Kong, in 1995, and is currently a Professor with the Department of Mechanical and Biomedical Engineering.

His current research interests include robot sensing, robot vision, three-dimensional vision, and visual tracking.

Prof. Li has served as an Associate Editor for the IEEE TRANSACTIONS ON AUTOMATION SCIENCE AND ENGINEERING and is currently an Associate Editor for the IEEE ROBOTICS AND AUTOMATION MAGAZINE. He is an Editor for the IEEE Robotics and Automation Society Conference Editorial Board and the IEEE Conference on Robotics and Automation.



Zengzhao Chen received the B.S. degree in computer science from Central China Normal University, Wuhan, China, in 1993, and the Ph.D. degree in computer application technology from the University of Science and Technology Beijing, Beijing, China, in 2007.

He is currently a Professor with the National Engineering Research Center for E-Learning, School in Central China Normal University, Wuhan. His research interests include educational information technology, image processing and pattern recognition, and human–computer interaction.



Zhaoli Zhang (M'18) received the M.S. degree in computer science from Central China Normal University, Wuhan, China, in 2004, and the Ph.D. degree in computer science from the Huazhong University of Science and Technology, Wuhan, in 2008.

He is currently a Professor with the National Engineering Research Center for E-Learning, School in Central China Normal University, Wuhan. His research interests include signal processing, knowledge services, and software

engineering. He is a Member of the IEEE and China Computer Federation.



Sannyuya Liu received the B.E., M.E., and Ph.D. degrees from the Huazhong University of Science and Technology, Wuhan, China, in 1996, 1999, and 2003, respectively.

From 2003 to 2005, he devoted himself to his postdoctoral research with Xiamen University, Xiamen Shi, China, and worked for the field of enterprise information, business intelligence, and distributed computing. He is currently a Professor with the National Engineering Research Center for E-Learning, School in Central China

Normal University, Wuhan. His research interests include artificial intelligence, computer application, machine learning, and educational data mining.